

# Probing Circumnuclear Environments with the HCN( $J = 3-2$ ) and $\text{HCO}^+$ ( $J = 3-2$ ) lines: Case of NGC 1097

Pei-Ying Hsieh<sup>1,2</sup>, Paul T. P. Ho<sup>1,3</sup>, Kotaro Kohno<sup>4,6</sup>, Chorng-Yuan Hwang<sup>2</sup>, Satoki Matsushita<sup>1,5</sup>

pyhsieh@asiaa.sinica.edu.tw

<sup>1</sup> *Academia Sinica Institute of Astronomy and Astrophysics, P.O. Box 23-141, Taipei 10617, Taiwan, R.O.C.*

<sup>2</sup> *Institute of Astronomy, National Central University, No.300, Zhongda Rd., Zhongli City, Taoyuan County 32001, Taiwan, R.O.C.*

<sup>3</sup> *Harvard-Smithsonian Center for Astrophysics, 60 Garden Street, Cambridge, MA 02138, USA*

<sup>4</sup> *Institute of Astronomy, The University of Tokyo, 2-21-1 Osawa, Mitaka-shi, Tokyo 181-0015*

<sup>5</sup> *Joint ALMA Office, Alonso de Córdova 3107, Vitacura 763 0355, Santiago, Chile*

<sup>6</sup> *Research Center for the Early Universe, University of Tokyo, 7-3-1 Hongo, Bunkyo, Tokyo 113-0033, Japan*

## ABSTRACT

We present the first interferometric HCN( $J = 3-2$ ) and  $\text{HCO}^+$ ( $J = 3-2$ ) maps in the circumnuclear region of NGC 1097, obtained with the Submillimeter Array. The goal is to study the characteristics of the dense gas associated with the starburst ring/Seyfert nucleus. With these transitions, we suppress the diffuse low density emission in the nuclear region. We detect and resolve the individual compact giant molecular cloud associations (GMAs) in the 1.4 kpc circumnuclear starburst ring and within the 350 pc nuclear region. The nucleus is brighter than the ring in both lines, and contributes to  $\sim 20\%$  and  $\sim 30\%$  to the total detected  $\text{HCO}^+$ ( $J = 3-2$ ) and HCN( $J = 3-2$ ) flux, within the central 1.4 kpc. The intensity ratios of HCN( $J = 3-2$ )/ $\text{HCO}^+$ ( $J = 3-2$ ) are roughly unity in the GMAs of the starburst ring. However, this ratio is up to  $\sim 2$  in the nuclear region. From the HCN( $J = 3-2$ )/HCN( $J = 1-0$ ) ratio of  $\leq 0.2$  in the nucleus,

we infer that the nuclear HCN( $J = 3-2$ ) emission might be optically thin. The  $\text{HCO}^+(J = 3-2)$  and HCN( $J = 3-2$ ) show correlations with  $^{12}\text{CO}(J = 3-2)$  and the  $24\mu\text{m}$  emission. The tight correlations of HCN( $J = 3-2$ ),  $\text{HCO}^+(J = 3-2)$  and  $24\mu\text{m}$  emission in the starburst ring suggest that the dense molecular gas and the dust are from the same origins of star forming regions. On the other hand, the HCN( $J = 3-2$ ) emission of the nucleus is significantly enhanced, indicating mechanisms other than star formation, such as AGN activities. A self-consistent check of the fractional abundance enhanced by X-ray ionization chemistry of the nucleus is possible with our observations.

*Subject headings:* Galaxies: individual (NGC 1097) – Galaxies: ISM – Galaxies: Seyfert – radio lines: ISM – Submillimeter: ISM – ISM : molecules

## 1. INTRODUCTION

HCN and  $\text{HCO}^+$  molecules are important dense gas tracers, which are readily detectable in external galaxies (e.g., Rickard et al. 1977; Nguyen-Q-Rieu et al. 1989; Jackson et al. 1993; Henkel et al. 1994; Paglione et al. 1995; Kohno et al. 2003; Gao & Solomon 2004; Riechers et al. 2006; García-Burillo et al. 2010), and in our own Galactic Center (e.g., Montero-Castaño et al. 2009). With their larger dipole moments, these rotational lines have higher critical densities than that of CO and hence are excellent probes of the dense cores within the molecular clouds. However, as the fractional abundance of HCN and  $\text{HCO}^+$  are usually 1000 times less than CO, these lines are correspondingly fainter. Nevertheless, extragalactic HCN emission lines conform to the well-known correlation with infrared emission over 7–8 orders of magnitude in sizescales (Gao & Solomon 2004; Wu et al. 2005). The HCN–IR luminosity has a tighter correlation than that of CO–IR (Solomon et al. 1992, 1997). This has been attributed to the fact that star formation occurs in dense gas rather than the diffuse gas traced by CO. However, in the extreme conditions of active galactic nuclei (AGN) and starbursts, HCN can be excited by the IR radiation rather than collisions (Aalto et al. 1995; Kohno et al. 2008; Sakamoto et al. 2010; García-Burillo et al. 2010), and the abundances of the HCN and  $\text{HCO}^+$  can be affected by the X-ray irradiation (Tacconi et al. 1994; Lepp & Dalgarno 1996; Usero et al. 2004; Meijerink & Spaans 2005; Meijerink et al. 2007; Imanishi et al. 2007; Kohno et al. 2008; Harada et al. 2010; García-Burillo et al. 2010). Early multi-J statistical studies of the extragalactic HCN and  $\text{HCO}^+$  were made by Krips et al. (2008) to study the molecular gas properties in AGNs and starbursts. The abundance and excitation of these molecules are indeed affected by the circumnuclear environments. Here, we focus on the  $J = 3-2$  transitions of HCN and  $\text{HCO}^+$ , which have  $\sim 30$  times larger dipole moments as

compared to CO, and have transition energy that are 6 times higher ( $\sim 26$  K) as compared to the  $J = 1-0$  transitions. Our purpose is to define the utility of these lines in the study of the dense and warm circumnuclear regions.

NGC 1097 is at a distance of 14.5 Mpc, and has a low luminosity-Seyfert nucleus and a circumnuclear starburst ring. The nucleus is prominent in X-ray, and is associated with a supermassive ( $\sim 10^8 M_\odot$ ) black hole (Lewis & Eracleous 2006; Nemmen et al. 2006). The circumnuclear starburst ring shows prominent continuum emission at cm, mid-IR, and far-IR wavelengths, with compact knots, which are associated with star formation at a SFR of  $5 M_\odot \text{ yr}^{-1}$  (Hummel et al. 1987; Sandstrom et al. 2010). The general properties of the circumnuclear molecular gas of CO, HCN, and  $\text{HCO}^+$  were studied with high resolution interferometers (Kohno et al. 2001, 2007; Hsieh et al. 2008, 2011). These lower- $J$  studies show a molecular ring and a nuclear concentration, which are coincident with the starburst ring and the Seyfert nucleus. The  $\text{HCN}(J = 1-0)$  enhancement in the nucleus relative to the ring, has been interpreted as an X-ray irradiation effect on the HCN abundance (Kohno et al. 2003, 2007). However, since the low- $J$  lines only trace the cold and diffuse gas, higher- $J$  lines may be better probes for the highly excited nuclear environments (e.g., Montero-Castaño et al. 2009; Matsushita et al. 2004). Here, we compare our first interferometric  $\text{HCN}(J = 3-2)$  and  $\text{HCO}^+(J = 3-2)$  maps of NGC 1097, at an angular resolution of  $\sim 4''$ , with the emission from the lower- $J$  transitions.

## 2. OBSERVATIONS AND DATA REDUCTION

We observed NGC 1097 with the Submillimeter Array<sup>1</sup> (Ho et al. 2004). Two nights of observations were obtained in 2008 and 2010 with the compact configuration and the 345 GHz receivers. The  $uv$ -coverages were  $\sim 7.5 - 61.5 k\lambda$  for both observations. The system temperatures ( $T_{\text{sys}}$ ) were  $\sim 150-300$  K and  $\sim 100-180$  K, respectively, for the two sessions.

The SMA correlator processes two IF sidebands separated by 10 GHz, with  $\sim 2$  GHz bandwidth each in 2008. The bandwidth was upgraded to 4 GHz bandwidth for each IF after 2009. The upper/lower sidebands were divided into slightly overlapping 24 and 48 chunks of 104 MHz width in 2008 and 2010, respectively. In 2008, we observed the  $\text{HCN}(J = 3-2)$  line (rest frequency: 265.886 GHz) in the LSB with 6 antennas. In 2010, we observed both the  $\text{HCN}(J = 3-2)$  and the  $\text{HCO}^+(J = 3-2)$  (rest frequency: 267.558 GHz) lines simultaneously

---

<sup>1</sup> The SMA is a joint project between the Smithsonian Astrophysical Observatory and the Academia Sinica Institute of Astronomy and Astrophysics and is funded by the Smithsonian Institution and the Academia Sinica.

in the LSB with 8 antennas because of the availability of the 4 GHz bandwidth.

We calibrated the SMA data with the MIR-IDL software package. The bandpass calibrators are 3C84, Uranus and Ceres for the first track, and 3C454.3 and 3C84 for the second track. Callisto and Uranus were used for the absolute flux calibration for the first and second dataset, respectively. The accuracy of the absolute flux calibration is  $\sim 15\%$  for both of the data. The gain calibrators are the quasars 0423–013 for the first track and 0137–245 (phase)/0403–360 (amplitude) for the second track, respectively. Mapping and analysis were done with the MIRIAD and the NRAO AIPS packages. We made the maps with natural weighting, and with the data binned to  $20 \text{ km s}^{-1}$  velocity resolution. The CLEAN processes were done in MIRIAD to remove the sidelobes. The synthesized beams are  $3''.7 \times 2''.6$  (PA =  $-10^\circ$ ) for the HCN(J = 3–2) maps and  $4''.4 \times 2''.6$  (PA =  $-15^\circ$ ) for the HCO<sup>+</sup>(J = 3–2) maps. For the latter comparisons of both lines, we convolved the maps to  $4''.4 \times 2''.7$  (PA =  $-14.6^\circ$ ). The  $1\sigma$  noise levels are  $11 \text{ mJy beam}^{-1}$  for both lines.

### 3. Results

#### 3.1. High Excitation Dense Gas in the Circumnuclear Region of NGC 1097

In Figure 1 we show the HCN(J = 3–2), HCO<sup>+</sup>(J = 3–2) and <sup>12</sup>CO(J = 3–2) (Hsieh et al. 2011) integrated intensity maps. The HCN(J = 3–2) and HCO<sup>+</sup>(J = 3–2) maps show a nuclear concentration and a molecular ring similar to the J = 1–0, J = 2–1, and the J = 3–2 CO maps (Kohno et al. 2003, 2007; Hsieh et al. 2008, 2011). The nucleus is the brightest feature in all the maps, and the relatively weaker molecular ring coincides with the starburst ring. The ring consists of GMAs at the scale of giant molecular cloud associations (GMAs) of 200–300 pc. However, since both of the HCN and HCO<sup>+</sup> lines have higher critical density than CO, the HCN and HCO<sup>+</sup> GMAs are expected to be the denser regions of the GMAs mapped in the previous CO lines. We identify a total of 8 GMAs including the one at the nucleus (Table 1). The GMAs are defined by the intensity peaks with visual inspection. We show the spectra of the nucleus in Figure 2. The spectra show asymmetric profiles, which are likely due to multiple underlying components. The blueshifted part is fainter than the redshifted part in all the lines.

The nucleus is brighter in HCN than HCO<sup>+</sup> in both the low- and high-J lines. HCN(J = 3–2) has better contrast between the nucleus and the starburst ring than CO(J = 3–2) and HCO<sup>+</sup>(J = 3–2). We demonstrate this by explicitly comparing the contribution of the emission from the nucleus and the molecular ring in these lines. The HCN(J = 3–2) integrated flux for the nucleus (radius:  $0''\text{--}6''$ ) and the ring (radius:  $6''\text{--}13''$ ) are  $34.4 \pm 3.4 \text{ Jy}$

km s<sup>-1</sup> and 89.9±6.7 Jy km s<sup>-1</sup>, respectively. Hence the nucleus contributes 30±3% of the HCN(J = 3–2) flux within 13″. The HCO<sup>+</sup>(J = 3–2) integrated flux of the nucleus and the ring are 17.4±3.4 Jy km s<sup>-1</sup> and 85.8±6.7 Jy km s<sup>-1</sup>, respectively. Therefore, the nucleus contributes 17±3% of the HCO<sup>+</sup>(J = 3–2) flux within 13″. The integrated <sup>12</sup>CO(J = 3–2) flux of the nucleus and ring are 1021 and 3778 Jy km s<sup>-1</sup>. Hence the nucleus contributes 21±0.2% of the total <sup>12</sup>CO(J = 3–2) flux within 13″. The HCN(J = 3–2) is therefore significantly brighter in the nuclear region as compared with the molecular ring.

### 3.2. Intensity Ratios of the Dense Gas in the Circumnuclear Region

We compare the HCN(J = 3–2), HCO<sup>+</sup>(J = 3–2), and <sup>12</sup>CO(J = 3–2) (Hsieh et al. 2011) at the angular resolution of 4″.4×2″.7. For the comparison of the J = 3–2 and J = 1–0 lines, we limited the shortest baselines to 7.5 kλ for all transitions, in order to match the resolution of the J = 1–0 lines at 7″.9×3″.2. HCN(J = 1–0), HCO<sup>+</sup>(J = 1–0), and <sup>12</sup>CO(J = 1–0) lines (Kohno et al. 2007, 2003, 2011) are included for these comparisons.

In Table 1, the averaged intensity ratios of HCN(J = 3–2)/HCO<sup>+</sup>(J = 3–2) are 1.11±0.36 and 2.13±0.34 in the ring and the nucleus, respectively. These values are similar to the single dish observations compiled by Krips et al. (2008), where the ratio is nearly unity in the starburst galaxies and larger than unity in the galaxies which host AGNs. The average intensity ratios of HCN(J = 3–2)/<sup>12</sup>CO(J = 3–2) are 0.05±0.01 and 0.07±0.01 in the ring and the nucleus, respectively. In Figure 3 we show the correlation of the fluxes of HCN(J = 3–2), HCO<sup>+</sup>(J = 3–2), and <sup>12</sup>CO(J = 3–2) lines. While there is a general correlation, the dispersion of these ratios within the molecular ring is about a factor of 2. We calculated the linear Pearson correlation coefficients of the plots in Figure 3. The correlation coefficients of all data are 0.86, 0.69, and 0.63 for Figure 3(a), (b), and (c) respectively. The correlation coefficients of the GMAs in the starburst ring are 0.74, 0.44, and 0.21 for Figure 3(a), (b), and (c). The higher coefficients represent stronger linear dependence of the two quantities. This variation in the molecular ring is responsible for the apparent differences between the GMAs in the ring. Such differences are marginally significant but difficult to interpret. Chemistry, excitation, and the contributions from diffuse gas to the CO(J = 3–2), may all be important.

We compare the ratios of J = 3–2 and J = 1–0 lines in low resolution (7″.9×3″.2) in Table 2. Kohno et al. (2001) reported that the lower-J line ratios of HCN(J = 1–0)/<sup>12</sup>CO(J = 1–0) is ~0.34, and the HCN(J = 1–0)/HCO<sup>+</sup>(J = 1–0) is ~2 in the nucleus. The HCN/HCO<sup>+</sup> seems to be similar in lower- and higher-J lines, while the HCN/<sup>12</sup>CO decreases toward the higher-J lines in the nucleus (0.04±0.01). The ring shows similar trends in Table 2. In both nucleus and ring, the HCO<sup>+</sup>/CO ratios decrease in J = 3–2. On the other hand, the

HCN(J = 3–2)/HCN(J = 1–0) and HCO<sup>+</sup>(J = 3–2)/HCO<sup>+</sup>(J = 1–0) ratios does not show significant difference in the ring and the nucleus. This result is consistent with the survey done by Krips et al. (2008). The decreasing HCN/CO ratios toward higher-J lines were reported in other galaxies host AGN, for instance, NGC 1068 (Krips et al. 2008, 2011), and M51 (Matsushita et al. 1998, 2004, 2007). We will discuss the physical conditions of the molecular gas in the Sect. 4.

We derive the line ratios in LTE conditions to roughly look into the effects of temperatures, opacities and abundance ratios on the HCN and HCO<sup>+</sup> lines. A more sophisticated radiative transfer model will be important once we have more lines and higher angular resolution. In our case, we are looking at the large scale properties of the molecular gas, and a simple LTE analysis is adequate since all the information are averaged by the coarse resolution. We define the brightness temperature  $T_B = f[J_\nu(T_{\text{ex}}) - J_\nu(T_{\text{bg}})](1 - e^{-\tau})$ , where  $T_B$  is the brightness temperature,  $f$  is the filling factor,  $J_\nu = (h\nu/k)(1/e^{h\nu/kT-1})$ ,  $T_{\text{ex}}$  is the excitation temperature,  $T_{\text{bg}}$  is the background temperature, and  $\tau$  is the opacity. In our estimates we assume the filling factors are the same for both lines. For the same molecular species at J = 3–2 and J = 1–0, the estimates are:

1. Both lines are optically thick ( $\tau \gg 1$ ), in which case the integrated intensity line ratio can be written as

$$R_{32/10}^{\text{thick}} = \frac{[J_{\nu_{32}}(T_{\text{ex}}) - J_{\nu_{32}}(T_{\text{bg}})]}{[J_{\nu_{10}}(T_{\text{ex}}) - J_{\nu_{10}}(T_{\text{bg}})]}, \quad (1)$$

where the background temperature  $T_{\text{bg}}$  is 2.7K. In LTE, the  $R_{32/10}$  approaches to unity with rising temperatures (see Figure 4a and Figure 5a).

2. Both lines are optically thin ( $\tau \ll 1$ ) and the integrated intensity line ratio can be written as

$$R_{32/10}^{\text{thin}} = \frac{[J_{\nu_{32}}(T_{\text{ex}}) - J_{\nu_{32}}(T_{\text{bg}})]\tau_{32}}{[J_{\nu_{10}}(T_{\text{ex}}) - J_{\nu_{10}}(T_{\text{bg}})]\tau_{10}}, \quad (2)$$

and

$$\frac{\tau_{32}}{\tau_{10}} = 3 \frac{\nu_{32}}{\nu_{10}} e^{-\frac{h\nu_{21}}{kT_{\text{ex}}}} e^{-\frac{h\nu_{10}}{kT_{\text{ex}}}} \frac{1 - e^{-h\nu_{32}/kT_{\text{ex}}}}{1 - e^{-h\nu_{10}/kT_{\text{ex}}}}, \quad (3)$$

which in LTE depends on the optical depth  $\tau$  at each frequency.  $\tau_{32}$  and  $\tau_{10}$  are the opacity of J = 3–2 and J = 1–0 lines. In Figures 4a and 5a, the ratio increases rapidly with  $T_{\text{ex}}$ .

3. We considered J = 3–2 line is optically thin and J = 1–0 line is optically thick

$$R_{32/10}^{\text{thin/thick}} = \frac{[J_{\nu_{32}}(T_{\text{ex}}) - J_{\nu_{32}}(T_{\text{bg}})]}{[J_{\nu_{10}}(T_{\text{ex}}) - J_{\nu_{10}}(T_{\text{bg}})]}\tau_{32}. \quad (4)$$

In Figure 4b and Figure 5b, we illustrate the dependence of the ratios on temperature and opacity, where the ratios of the same molecules are independent of the abundance. In both figures, the ratios seem to be more sensitive to the temperatures when  $T_{\text{ex}} \leq 20\text{K}$ , but are dependent on the opacity of  $\text{HCN}(J = 3-2)$  and  $\text{HCO}^+(J = 3-2)$  at  $T_{\text{ex}} \geq 20\text{K}$ . This dependence of temperature/opacity also varies with ratios.

The ratios of  $^{12}\text{CO}(J = 3-2)/^{12}\text{CO}(J = 1-0)$  lines are shown in Table 2. We also derive the LTE results of the  $^{12}\text{CO}(J = 3-2)/^{12}\text{CO}(J = 1-0)$  ratios in Figure 6. The first two cases in Figure 6a are for when both lines are optically thick and optically thin. The third case (Figure 6b) is assuming optically thin  $^{12}\text{CO}(J = 1-0)$  and optically thick  $^{12}\text{CO}(J = 3-2)$  lines.

For the ratios of the different species of  $\text{HCN}(J = 3-2)$  and  $\text{HCO}^+(J = 3-2)$ , we illustrate the two cases when both lines are optically thick and thin:

1. Both lines are optically thick ( $\tau \gg 1$ ), in which case the integrated intensity line ratio can be written as

$$R_{\text{HCN}/\text{HCO}^+}^{\text{thick}} = \frac{[J_{\text{HCN}}(T_{\text{ex}}) - J_{\text{HCN}}(T_{\text{bg}})]}{[J_{\text{HCO}^+}(T_{\text{ex}}) - J_{\text{HCO}^+}(T_{\text{bg}})]}. \quad (5)$$

The ratios quickly saturate to nearly unity (see Figure 7a and Figure 7a) in the case when both lines are thick.

2. Both lines are optically thin ( $\tau \ll 1$ ) and the integrated intensity line ratio can be written as

$$R_{\text{HCN}/\text{HCO}^+}^{\text{thin}} = \frac{[J_{\text{HCN}}(T_{\text{ex}}) - J_{\text{HCN}}(T_{\text{bg}})]\tau_{\text{HCN}}}{[J_{\text{HCO}^+}(T_{\text{ex}}) - J_{\text{HCO}^+}(T_{\text{bg}})]\tau_{\text{HCO}^+}}, \quad (6)$$

and

$$\frac{\tau_{\text{HCN}}}{\tau_{\text{HCO}^+}} = \frac{\nu_{\text{HCO}^+32}^2}{\nu_{\text{HCN}32}^2} \frac{N_{\text{HCN}}}{N_{\text{HCO}^+}} \frac{B_{\text{HCN}32}}{B_{\text{HCO}^+32}} \frac{e^{-\frac{6hB_{\text{HCN}32}}{kT_{\text{ex}}}}}{e^{-\frac{6hB_{\text{HCO}^+32}}{kT_{\text{ex}}}}} \frac{A_{\text{HCN}32}}{A_{\text{HCO}^+32}} \frac{1 - e^{-h\nu_{\text{HCN}}/kT_{\text{ex}}}}{1 - e^{-h\nu_{\text{HCO}^+}/kT_{\text{ex}}}}, \quad (7)$$

which in LTE depends on the optical depth  $\tau$  at each frequency.  $\tau_{\text{HCN}}$  and  $\tau_{\text{HCO}^+}$  represent the opacity of  $\text{HCN}(J = 3-2)$  and  $\text{HCO}^+(J = 3-2)$  lines. The  $B_{\text{HCN}32}$  and  $B_{\text{HCO}^+32}$  are the rotational constants of HCN and  $\text{HCO}^+$ .  $A_{\text{HCN}32}$  and  $A_{\text{HCO}^+32}$  are the Einstein A coefficients of  $\text{HCN}(J = 3-2)$  and  $\text{HCO}^+(J = 3-2)$ .  $N_{\text{HCN}}$  and  $N_{\text{HCO}^+}$  are the total column density of HCN and  $\text{HCO}^+$  molecules. Therefore the free parameters are the column density ratio, which is proportional to the abundance ratio of the HCN and  $\text{HCO}^+$  molecules if their size scales and the excitation temperature  $T_{\text{ex}}$  are similar. In Figure 7b, we show the  $\text{HCN}(J = 3-2)/\text{HCO}^+(J = 3-2)$  ratios as a function of  $T_{\text{ex}}$  and  $\text{HCN}/\text{HCO}^+$  abundance ratio. The line ratios are nearly insensitive to the temperatures, but are dependent on the abundance ratios.

### 3.3. Correlation of the molecular line intensity and 24 $\mu$ m continuum

In Figure 8 we show the comparison of the molecular gas and the archival Spitzer 24 $\mu$ m continuum emission. The PSF of the 24 $\mu$ m map is  $\sim 6''$ , and we smoothed our molecular line maps to match this resolution. In Figure 9 we show the relation of the molecular line intensity with the 24 $\mu$ m continuum emission for the GMAs. In Figure 9(a), the HCN( $J = 3-2$ ) flux of the ring seems to be tightly correlated to the 24 $\mu$ m continuum emission, while the nuclear emission is offset from this correlation. The relation is less tight for the lower critical density lines of HCO $^+$ ( $J = 3-2$ ) and  $^{12}\text{CO}$ ( $J = 3-2$ ). However, for these lines, the nuclear emission is closer to the correlation of the ring. We calculated the linear Pearson correlation coefficients of the plots in Figure 9. The correlation coefficients of all data are  $-0.23$ ,  $0.26$ , and  $-0.10$  for Figure 9(a), (b), and (c) respectively. The correlation coefficients of the GMAs in the starburst ring are  $0.86$ ,  $0.51$ , and  $0.36$  for Figure 9(a), (b), and (c). In this case, including the nucleus will decrease the linear dependence of the two quantities.

## 4. DISCUSSIONS

The nucleus of NGC 1097 seems to have environments of higher excitation than the ring. Our spatially resolved HCN( $J = 3-2$ ) and HCO $^+$ ( $J = 3-2$ ) maps show that the nucleus is brighter than the molecular ring. Similar results have also been shown in other interferometric studies of multi- $J$  HCN/HCO $^+$  emission such as M51 and NGC 1068 (Matsushita et al. 1998, 2004, 2007; Krips et al. 2011). The ratio of upper transition as compared to lower transitions, on the other hand, does not show a sharp enhancement in the nuclear region. The nature of the higher excitation in the nucleus can thus be deduced as following discussions. The necessity of analysis with multiple transitions has already been indicated from the previous studies by Kohno et al. (2003) and the single dish survey by Krips et al. (2008) toward nearby active/starburst galaxies. In this paper, we discuss our results with standard LTE analysis.

### 4.1. Physical Properties of the $J = 3-2$ lines

In Sect. 3.2 we derived the LTE estimates of the physical parameters for the HCN and HCO $^+$  molecules. In Figures 4a and 5a, if the HCN( $J = 3-2$ ), HCN( $J = 1-0$ ), HCO $^+$ ( $J = 3-2$ ), and HCO $^+$ ( $J = 1-0$ ) lines are optically thick, which suggests cold/thick dense molecular gas in both the nucleus and the ring with  $T_{\text{ex}} \sim 5\text{K}$ . This is possible since our spatial resolution is still quite coarse at 300 pc, so that we are likely sampling extended and colder



material. However, since the optically thick molecular gas has typical temperature of  $\geq 10\text{K}$  (Dishoeck et al. 1993), while the observed  $\text{HCN}(J = 3-2)/\text{HCN}(J = 1-0)$  and  $\text{HCO}^+(J = 3-2)/\text{HCO}^+(J = 1-0)$  ratios are lower than LTE estimates of  $\sim 0.5$  at 10K. The inconsistency may be either the four lines are not all optically thick, or the different filling factors of those transitions.

In Figure 7a, the  $\text{HCN}_{32}/\text{HCO}_{32}^+$  ratio is nearly unity if both lines are thick. This is consistent with the average ratio of the ring, but inconsistent for the nucleus. Therefore, both  $\text{HCN}(J = 3-2)$  and  $\text{HCO}^+(J = 3-2)$  being optically thick is less likely for the nucleus. This case can not be ruled out since we do not have a promising optically thin line to determine the physical parameters. Alternatively, that the  $J = 3-2$  lines are weaker than the  $J = 1-0$  lines, may be because the  $J = 3-2$  lines are thin and  $J = 1-0$  lines are thick. As it is shown in Figures 4b and 5b, the line ratios depend on the  $J = 3-2$  opacity and  $T_{\text{ex}}$ . Note that the  $J = 3-2$  to  $J = 1-0$  ratios for the nucleus and the ring, are similar within the uncertainties. The LTE estimates suggest that the  $J = 3-2$  lines may be colder with higher opacity or warmer with lower opacity.

In the case where both  $\text{HCN}(J = 3-2)$  and  $\text{HCO}^+(J = 3-2)$  are optically thin, we could estimate the abundance ratio of  $\text{HCN}/\text{HCO}^+$  in Figure 7b. The  $[\text{HCN}]/[\text{HCO}^+]$  ratio is  $\sim 2.5 - 4.5$  and  $\sim 1 - 3$  for the nucleus and the ring. The optically thin scenarios seem to be supported by Figure 9a,b, which show tighter correlations with the  $24\mu\text{m}$  emission at GMAs scale. The tighter relations of  $\text{HCN}(J = 3-2)$ , and  $\text{HCO}^+(J = 3-2)$  with  $24\mu\text{m}$  emissions suggest these two lines trace the star forming regions better than  $\text{CO}(J = 3-2)$  line. If the  $\text{HCN}(J = 3-2)$ ,  $\text{HCO}^+(J = 3-2)$ , and  $24\mu\text{m}$  emissions are optically thin, their fluxes will be proportional to the column density of molecular gas and dust. Their good correlations may reflect that these are reliable tracers of the mass. On the other hand, the abundant molecule of CO is likely to remain optically thick in the  $J = 3-2$  line, which leads to a poor relation in Figure 9c. We note that the enhancement of the  $\text{HCN}(J = 3-2)$  emission in the nucleus is not simple. The  $\text{HCN}(J = 3-2)$  has a factor of two excess flux as compared to the  $\text{HCO}^+(J = 3-2)$ . This excess is likely due to the different abundance ratio of the HCN and  $\text{HCO}^+$  in the ring and the nucleus as it is shown in Figure 7b. The abundance ratio would depend on the different physical environments, and we will discuss the effects of the chemistry in the following section.

On the contrary to the low  $\text{HCN}(J = 3-2)/\text{HCO}^+(J = 3-2)$  ratios, the high  $^{12}\text{CO}(J = 3-2)/^{12}\text{CO}(J = 1-0)$  ratios in the circumnuclear region of NGC 1097 seem to suggest that the  $^{12}\text{CO}(J = 3-2)$  line is optically thick, and the  $^{12}\text{CO}(J = 1-0)$  is optically thin (Figure 6). The similar high ratios  $\geq 2$  were also reported in NGC 1068 (Krips et al. 2011; Tsai et al. 2011) and M51 (Matsushita et al. 2004). In Figure 6, for the case of  $^{12}\text{CO}(J = 3-2)/^{12}\text{CO}(J$

$= 1-0$ ) ratios larger than unity, the higher  $T_{\text{ex}}$  or lower opacity of  $^{12}\text{CO}(J = 1-0)$  line lead to the higher  $^{12}\text{CO}(J = 3-2)/^{12}\text{CO}(J = 1-0)$  ratios. Given the similar  $^{12}\text{CO}(J = 1-0)$  opacity of the nucleus and the molecular ring, the higher  $^{12}\text{CO}(J = 3-2)/^{12}\text{CO}(J = 1-0)$  ratio of the nucleus suggests it has higher temperature than the ring, or the nucleus has lower  $^{12}\text{CO}(J = 1-0)$  opacity than the ring. These factors might also be consistent with the decreasing HCN/CO ratios toward high- $J$  lines reported in the previous studies by Krips et al. (2008, 2011). Note that the LTE analysis gives the simplified results since the ratios also depend on other physical parameters such as gas density. Unfortunately, the LTE analysis can not provide straightforward density solution. This is because we need additional information such as fractional abundance and source size. However, in principle we expect in the case of collisional excitation, higher density conditions might increase the higher- $J$  population of molecules.

In terms of excitation, the observed low values for the ratios of  $\text{HCN}(J = 3-2)/\text{HCN}(J = 1-0)$  and  $\text{HCO}^+(J = 3-2)/\text{HCO}^+(J = 1-0)$  also suggest that the  $J = 3-2$  transitions might be subthermal. The case of subthermal excitation for the higher- $J$  HCN/HCO<sup>+</sup> lines has also been found in other galaxies (e.g., Nguyen-Q-Rieu et al. 1992; Riechers et al. 2011). The critical density is defined when the molecules are in thermal equilibrium via collisions. Densities have to be higher in order to drive the collisional time scale to be significantly shorter than the spontaneous decay time scale as defined by the Einstein A coefficient, in order to populate the upper energy levels. Since the Einstein A coefficient scales as  $\nu^3$ , the rapid spontaneous decay rate will eventually overwhelm the collision rate for a sufficiently high energy state. In such case, the subthermally excited lines will set an upper limit on the densities as compared to the critical density of the particular transitions. Based on the bright HCN/HCO<sup>+</sup>  $J = 3-2$  emission, and their low intensity ratio as compared to the lower transitions, the low density scenario with subthermal excitation, is also possible. However, the high  $^{12}\text{CO}(J = 3-2)/^{12}\text{CO}(J = 1-0)$  ratios of the circumnuclear region in NGC 1097 might suggest high gas density, which is in conflict to the above scenario. A careful excitation analysis cooperating with multi- $J$  molecular lines are essential to derive the gas density, excitation temperature, and kinetic temperature to examine the possibility of subthermal conditions of  $J = 3-2$  HCN, HCO<sup>+</sup> lines, such as the works done by Krips et al. (2008, 2011).

#### 4.2. Column Density of the HCN and HCO<sup>+</sup> molecules

We can calculate the column density of HCN and HCO<sup>+</sup> by assuming LTE conditions and correcting for the optical depth,

$$N_{mol} = \frac{3k}{8\pi^3 B_{rot} \mu^2} \frac{e^{hB_{rot} J_l(J_l+1)/kT_{ex}}}{J_l + 1} \frac{(T_{ex} + hB_{rot}/3k)}{(h\nu/k)e^{-h\nu/kT_{ex}}} \frac{\tau_\nu}{1 - e^{-\tau_\nu}} \int T_b dv, \quad (8)$$

where  $N_{mol}$  is the column density of specific molecule,  $k$  and  $h$  are the Boltzmann and Planck constants,  $B_{rot}$  is the rotational constant of the molecule,  $\mu$  is the electric dipole moment of the molecule,  $J_l$  is the quantum number of the lower energy level from  $J + 1 \rightarrow J$ ,  $T_{ex}$  is the excitation temperature which is constant under LTE assumption for all transitions,  $\tau_\nu$  is the opacity, and  $dv$  is the velocity width. The column density of  $H_2$  can then be derived from the abundance ratio of [Molecule]/[ $H_2$ ]. Alternatively, if we derive the column density of  $H_2$  from other observations, we can estimate the abundances of HCN and  $HCO^+$ . We calculate  $B_{rot}$  of HCN and  $HCO^+$  to be 44.31 and 44.59 GHz. The values of  $\mu$  for HCN and  $HCO^+$  are  $2.98 \times 10^{-18}$  and  $3.92 \times 10^{-18}$  e.s.u. cm. We then calculate  $N_{HCN}$  and  $N_{HCO^+}$  by

$$N_{HCN} = 1.108 \times 10^{10} \frac{(T_{ex} + 0.709)}{e^{-25.525/T_{ex}}} \frac{\tau_\nu}{1 - e^{-\tau_\nu}} \int T_b(HCN(J = 3 - 2)) dv, \quad (9)$$

$$N_{HCO^+} = 6.325 \times 10^9 \frac{(T_{ex} + 0.713)}{e^{-25.685/T_{ex}}} \frac{\tau_\nu}{1 - e^{-\tau_\nu}} \int T_b(HCO^+(J = 3 - 2)) dv, \quad (10)$$

We estimate the cases of the nucleus and the ring separately with different temperatures and opacities. As for the nucleus, we adopt the warm and thin conditions based on the previous discussions. In terms of temperatures, Sandstrom et al. (2010) fitted the SED of the nucleus of NGC 1097 for the spatial scale of 600 pc, and found that the thermal blackbody spectrum peaks at  $\sim 100\mu m$ , corresponding to a dust temperature of  $T_d \sim 30K$ . However, an additional peak seems to be located at  $\sim 10\mu m$ , where corresponds to  $T_d$  of  $\sim 300K$ . We thus constrain the range of the  $N_{HCN}$  within this range. Since the opacities are nearly constant from 30 to 300 K (Figure 4b), the corresponding opacities of HCN( $J = 3-2$ ) and  $HCO^+(J = 3-2)$  are  $\sim 0.2$  in this range. Then  $N_{HCN}$  is  $\sim 2 \times 10^{13}$  to  $1 \times 10^{14} \text{ cm}^{-2}$ , and  $N_{HCO^+}$  is  $\sim 6 \times 10^{12}$  to  $3 \times 10^{13} \text{ cm}^{-2}$ . The column density of  $H_2$  in the nucleus, as derived from CO( $J = 3-2$ ) (Table 1) with a conversion factor of  $1.8 \times 10^{20} (\text{K km s}^{-1})^{-1} \text{ cm}^{-2}$  (Dame et al. 2001), is  $3 \times 10^{22} \text{ cm}^{-2}$ . If we adopt this value for the total  $H_2$  column density, we can estimate the fractional abundance of HCN and  $HCO^+$ . We find  $N_{HCN}/N_{H_2}$  is  $7 \times 10^{-10}$  to  $3 \times 10^{-9}$ , and  $N_{HCO^+}/N_{H_2}$  is  $2 \times 10^{-10}$  to  $9 \times 10^{-10}$ . The conversion factor in the galactic center was suggested to be lower than the value of galactic disk. Mauersberger et al. (1996) suggests that the conversion factor is  $0.3 \times 10^{20} (\text{K km s}^{-1})^{-1} \text{ cm}^{-2}$  in the nuclear starburst environments. Hence the abundances mentioned above would be larger by a factor of 6. The key uncertainty here is whether the CO, HCN, and  $HCO^+$ , are spatially coextensive. The derived column density ratios are the mean values averaged over the volume of the CO

emission. Another route to estimate the  $[\text{HCN}]/[\text{H}_2]$  is to adopt the  $N_{\text{H}_2}$  as derived from the X-ray absorption. The  $N_{\text{H}_2}$  of the nucleus as derived by Nemmen et al. (2006) is  $4.6 \times 10^{20} \text{ cm}^{-2}$ , which increases the  $[\text{HCN}]/[\text{H}_2]$  and  $[\text{HCO}^+]/[\text{H}_2]$  by a factor of  $\sim 60$ .

As for the molecular star-forming ring, using the same analysis, with a temperature of 30 K, and opacities of 0.2, we derive  $N_{\text{H}_2}$  for the ring-GMAs of  $3 \times 10^{22} \text{ cm}^{-2}$ ,  $N_{\text{HCN}}$  of  $\sim 7 \times 10^{12} \text{ cm}^{-2}$ , and  $N_{\text{HCO}^+}$  of  $\sim 4 \times 10^{12} \text{ cm}^{-2}$ . The  $[\text{HCN}]/[\text{H}_2]$  and  $[\text{HCO}^+]/[\text{H}_2]$  are  $2 \times 10^{-10}$  and  $1 \times 10^{-10}$ , respectively.

CO is usually optically thick because of its large abundance and low critical density. The concern is that we may sample the cold gas on the surface of the molecular clouds with CO, while the HCN and  $\text{HCO}^+$  sample the inner region of the clouds. The  $\text{H}_2$  column density as derived from the X-ray absorption may be more appropriate if the X-ray traces the more compact and denser regions. We thus favor the larger fractional abundance as estimated above via the X-ray absorption.

### 4.3. Chemical Abundances in the Nucleus

We can check if these chemical abundances are consistent with the ionization chemistry as suggested in the classical studies of Lepp & Dalgarno (1996). These authors predicted the fractional abundance of molecules for various ionizing densities (see their Fig. 2, 3). The ionizing flux densities was defined by  $\xi/n_{\text{H}_2}$  ( $\text{erg s}^{-1} \text{ cm}^{-3}$ ) in their paper, where  $\xi$  and  $n_{\text{H}_2}$  are the ionization rate and the volume number density of the molecular hydrogen. If the ionizing flux is dominated by the X-ray emission in the nucleus, its luminosity within the energy range of 2–10 KeV is  $4.4 \times 10^{40} \text{ erg s}^{-1}$  (Nemmen et al. 2006). Maloney et al. (1996) derived the X-ray ionization rate in the low-ionization limit as  $\xi \sim 1.4 \times 10^{-11} L_{44} r_2^{-2} N_{22}^{-1} (\text{s}^{-1})$ , where  $L_{44}$ ,  $r_2$ ,  $N_{22}$  are the X-ray luminosity in unit of  $10^{44} \text{ erg s}^{-1}$ , the distance to the X-ray source in the unit of 100 pc, and the  $\text{H}_2$  column density attenuating the X-ray flux in the unit of  $10^{22} \text{ cm}^{-2}$ . We assume the ionization radiation has an isotropic distribution, and we adopt the  $N_{\text{H}_2}$  as derived from CO of  $3 \times 10^{22} \text{ cm}^{-2}$  at the radius of  $1''.6 = 126 \text{ pc}$  (the average half width of the synthesized beam). This gives  $\xi$  of  $1.3 \times 10^{-15} \text{ s}^{-1}$ . We have also estimated that  $n_{\text{H}_2}$  of the nucleus is  $10^{4 \pm 1} \text{ cm}^{-3}$  (Hsieh et al. 2008). Hence  $\log \xi/n_{\text{H}_2}$  is  $-17.9$  to  $-19.9$ . For the other case of the  $N_{\text{H}_2}$  estimated from the X-ray absorption, the corresponding  $\xi$  is  $10^{-13} \text{ s}^{-1}$  and the  $\log \xi/n_{\text{H}_2}$  is  $-15.9$  to  $-17.9$ . The HCN fractional abundance predicted by the model corresponds to the range estimated by CO and X-ray absorption are  $-8.7$  to  $-7.4$  and  $\leq -7.8$ , respectively. Thus, the HCN abundance predicted by the X-ray ionization chemistry is consistent with both cases we estimated above. However, if it favors the latter case, a larger  $\text{H}_2$  number density is probably required to generate the higher HCN abundance. We

also find that the  $\text{HCO}^+$  abundance is consistent with the X-ray ionization chemistry for the case of  $N_{\text{H}_2}$  as derived from X-ray absorption. We conclude from our  $J = 3-2$  high resolution studies, that the X-ray ionization chemistry can explain the physical conditions in the nucleus.

## 5. SUMMARY

1. We detected the  $J = 3-2$  HCN,  $\text{HCO}^+$  lines in the circumnuclear region of NGC 1097. The HCN and  $\text{HCO}^+$  lines reveal a bright nucleus as compared to the molecular ring. The HCN( $J = 3-2$ ) lines contribute  $\sim 30\%$  of the total flux to the nucleus, while it is only  $\sim 20\%$  for the  $\text{HCO}^+(J = 3-2)$  and CO( $J = 3-2$ ) lines. The HCN( $J = 3-2$ )/ $\text{HCO}^+(J = 3-2)$  has a value of 2 in the nucleus and unity in the ring. The  $J = 3-2$  to  $J = 1-0$  ratios of both lines are as low as  $\sim 0.2$  for both the nucleus and the ring. Our results generally agree with the previous single dish surveys.
2. Our standard LTE analysis suggests that the HCN( $J = 3-2$ ) and  $\text{HCO}^+(J = 3-2)$  lines might be optically thin in the nucleus. Both lines can be optically thin or thick in the molecular ring. The high- $J$  lines with larger critical density, however, might also be subthermally excited. The tight correlation of the flux of HCN and  $\text{HCO}^+$  and  $24\mu\text{m}$  emission suggest these two lines trace the same origins of star formation in the ring better than CO, while other mechanisms such as AGN activities contribute to the HCN enhancements in the nucleus.
3. The simple estimates of the self-consistency of the X-ray ionization chemistry is made with our high- $J$  observations. The results suggest that the ionization chemistry model can explain the excess of the HCN abundance in the nucleus.

We thank for the SMA staffs for the SMA operations for this project. We acknowledge the anonymous referee for the stimulating comments to improve the manuscript. P.-Y. Hsieh acknowledges Dr. Tatsuhiko Hasegawa to complete this project.

## REFERENCES

- Aalto, S., Booth, R. S., Black, J. H. & Johansson, L. E. B. 1995, *A&A*, 300, 369
- Dame, T. M., H., Dap, T., P 2001 *ApJ*, 547, 792
- Dishoeck, E.F. van, Blake, G.A., Draine, B.T., Lunine, J.I. 1993, *Protostellar and Protoplanetary Matter in Protostars and Planets III*, Levy, E.H., Lunine, J.I. eds. University of Arizona Press: Tucson, p. 163
- Lepp, S., & Dalgarno, A. 1996, *A&A*, 306, 21
- García-Burillo, S.; Usero, A.; Fuente, A.; Martín-Pintado, J.; Boone, F.; Aalto, S.; Krips, M.; Neri, R.; Schinnerer, E.; Tacconi, L. J. 2010, *A&A*, 519, 2
- Gao, Y., Solomon, P. M. 2004, *ApJS*, 152, 63
- Harada, Nanase; Herbst, Eric; Wakelam, Valentine 2010, *ApJ*, 721, 1570
- Henkel, C.; Whiteoak, J. B.; Mauersberger, R. 1994, *A&A*, 284, 17
- Ho, P. T. P., Moran, J. M., & Lo, F. 2004, *ApJ*, 616, L1
- Hsieh, P.-Y., Matsushita, S., Lim, J., Kohno, K., & Sawada-Satoh, S. 2008, *ApJ*, 683, 70
- Hsieh, P.-Y., Matsushita, S., Liu, G., Ho, P. T. P., Nagisa, O., & Wu, Y.-L. 2011, *ApJ*, 736, 129
- Hummel, E., van der Hulst, J. M., Keel, W. C. 1987, *A&A*, 172, 32
- Imanishi, Masatoshi; Nakanishi, Kouichiro; Tamura, Yoichi; Oi, Nagisa; Kohno, Kotaro 2007, *AJ*, 134, 2366
- Jackson, James M.; Paglione, Timothy A. D.; Ishizuki, Sumio; Nguyen-Q-Rieu 1993, *ApJ*, 418, 13
- Kohno, K. 2001, *ASPC*, 289, 349
- Kohno, K., Ishizuki, S., Matsushita, S., Vila-Vilaró, B., & Kawabe, R. 2003, *PASJ*, 55, 1
- Kohno, K.; Nakanishi, K.; Imanishi, M. 2007, *ASPC*, 373, 647
- Kohno, Kotaro; Nakanishi, Koichiro; Tosaki, Tomoka; Muraoka, Kazuyuki; Miura, Rie; Ezawa, Hajime; Kawabe, Ryohei 2008, *Ap&SS*.313, 279

- Kohno, K et al. 2011, in preparation.
- Krips, M.; Neri, R.; Graciá-Burillo, S; Martín, S.; Combes, F.; Graciá-Carpio, J.; Eckart, A. 2008, *ApJ*, 677, 262
- Krips, M. et al. 2011, *ApJ*, 736, 37
- Lepp, S, & Dalgarno, A. 1996, *A&A*, 306, 21
- Lewis, K. T., Eracleous, M. 2006, *ApJ*, 642, 711
- Meijerink, R., & Spaans, M. 2005, *A&A*, 436, 397
- Meijerink, R., Spaans, M., Israel, F. P. 2007, *A&A*, 461, 793
- Matsushita, S., Kohno, K., Vila-Vilaro, B., Tosaki, T., Kawabe, R. 1998, *ApJ*, 495, 267
- Matsushita, S. et al. 2004, *ApJ*, 616, 55
- Matsushita, S., Muller, S., Lim, J. 2007, *A&A*, 468, 49
- Maloney, P. R., Hollenbach, D. J., & Tielens, A. G. G. M. 1996, *ApJ*, 466, 561
- Mauersberger, R., Henkel, C., Wielebinski, R., Wiklind, T., Reuter, H.-P. 1996, *A&A*, 305, 421
- Montero–Castaño, M., Hernstein, R. M. & Ho, P. T.-P. 2009, *ApJ*, 695, 1477
- Nemmen, R. S., Storchi-Bergmann, T., Yuan, F., Eracleous, M., Terashima, Y., Wilson, A. S. 2006, *ApJ*, 643, 652
- Nguyen-Q-Rieu, N. Nakai, & J. M. Jackson 1989, *A&A*, 220, 57
- Nguyen-Q-Rieu, N. Nakai, & J. M. Jackson, Henkel, C., Truong-Bach, & Mauersberger, R. 1992, *A&A*, 399, 521
- Nemmen, R. S., Storchi-Bergmann, T., Y., Feng, Eracleous, M., Terashima, Y., Wilson, A. S. 2006, *ApJ*, 643, 652
- Paglionie, Timothy A. D.; Tosaki, Tomoka; Jackson, James M. 1995, *ApJ*, 454, 117
- Riechers, Dominik A., Walter, Fabian, Carilli, Christopher L., Cox, Pierre, Weiss, Axel, Bertoldi, Frank, & Menten, Karl M. 2011, *ApJ*, 726, 50
- Riechers, Dominik A.; Walter, Fabian; Carilli, Christopher L.; Weiss, Axel; Bertoldi, Frank; Menten, Karl M.; Knudsen, Kirsten K.; Cox, Pierre 2006, *ApJ*, 645, 13

- Rickard, L. J., Turner, B. E., Palmer, P., Morris, M., & Zuckerman, B. 1977, *ApJ*, 214, 390
- Sandstrom, K. et al. 2010, *A&A*, 518, 59
- Sakamoto, K., Aalto, S., Evans, A. S., Wiedner, M. C., & Wilner, D. J. 2010, *ApJ*, 725, 228
- Solomon, P. M., Downes, D., Radford, S. J. E. 1992, *ApJ*, 387, 55
- Solomon, P. M., Downes, D., Radford, S. J. E., & Barrett, J. W. 1997, *ApJ*, 478, 144
- Tacconi, L. J.; Genzel, R.; Blietz, M.; Cameron, M.; Harris, A. I.; Madden, S. 1994, *ApJ*, 426, 77
- Tsai, M.-C., Hwang, C.-Y., Matsushita, S., Baker, A. J., Espada, D. 2011, *ApJ*, in press
- Usero, A.; Garca-Burillo, S.; Fuente, A.; Martn-Pintado, J.; Rodrguez-Fernndez, N. J. 2004, *A&A*, 419, 897
- Wu, J., Evans, N. J., II, Gao, Y., Solomon, P. M., Shirley, Y. L., Vanden B., & Paul A. 2005, *ApJ*, 635, 173



Table 1. Ratios at high angular resolution

GMA	Positions	HCN(J = 3–2) (1) (K km s <sup>−1</sup> )	HCO <sup>+</sup> (J = 3–2) (2) (K km s <sup>−1</sup> )	<sup>12</sup> CO(J = 3–2) (3) (K km s <sup>−1</sup> )	HCN <sub>32</sub> /HCO <sup>+</sup> <sub>32</sub> (4)	HCN <sub>32</sub> / <sup>12</sup> CO <sub>32</sub> (5)	HCO <sup>+</sup> <sub>32</sub> / <sup>12</sup> CO <sub>32</sub> (6)
1	3''0,9''5	10.8	8.1	189.0	1.33±0.34	0.05±0.01	0.05±0.01
2	−5''0,7''5	7.6	5.2	120.9	1.47±0.57	0.06±0.01	0.05±0.01
3	−8''5,−3''0	9.5	8.5	273.4	1.11±0.29	0.03±0.01	0.04±0.01
4	−5''0,−8''0	7.9	7.5	159.5	1.06±0.32	0.04±0.01	0.04±0.01
5	1''0,−9''0	6.4	4.8	110.4	1.36±0.59	0.06±0.02	0.06±0.02
6	8''5,−6''5	6.0	9.7	121.9	0.62±0.20	0.04±0.01	0.06±0.01
7	8''5,4''0	8.1	9.7	175.3	0.84±0.22	0.04±0.01	0.05±0.01
8	0''5,0''0	24.7	11.6	336.1	2.13±0.34	0.07±0.01	0.04±0.01

Note. — The flux density of the peaks are measured within one synthesized beam (4''4×2''7). The (δR.A.,δDecl.) position of the peaks relative to the phase center. The uncertainties of the HCN(J = 3–2), HCO<sup>+</sup>(J = 3–2), and CO(J = 3–2) are 1.7 K km s<sup>−1</sup>, 1.7 K km s<sup>−1</sup>, and 3.6 K km s<sup>−1</sup>, respectively.

Table 2. Ratios at low angular resolution

Ratios	Nucleus (1)	Ring (2)
HCN <sub>10</sub> /HCO <sup>+</sup> <sub>10</sub>	2.22±0.50	1.67±0.83
HCN <sub>10</sub> /CO <sub>10</sub>	0.59±0.13	0.35±0.14
HCO <sup>+</sup> <sub>10</sub> /CO <sub>10</sub>	0.27±0.07	0.21±0.11
HCN <sub>32</sub> /HCO <sup>+</sup> <sub>32</sub>	2.01±0.41	1.07±0.48
HCN <sub>32</sub> /CO <sub>32</sub>	0.04±0.01	0.02±0.01
HCO <sup>+</sup> <sub>32</sub> /CO <sub>32</sub>	0.02±0.01	0.02±0.01
HCN <sub>32</sub> /HCN <sub>10</sub>	0.15±0.02	0.12±0.05
HCO <sup>+</sup> <sub>32</sub> /HCO <sup>+</sup> <sub>10</sub>	0.17±0.05	0.19±0.10
<sup>12</sup> CO <sub>32</sub> / <sup>12</sup> CO <sub>10</sub>	2.33±0.44	1.84±0.56

Note. — In this table, we show the low resolution (7''9×3''2) intensity ratios of the nucleus and ring. The ratio of the nucleus is measured at the intensity peak. We measured the azimuthally averaged intensity ratios of the ring within radius of 6''–13''.

Table 3. Comparisons of flux of  $24\mu\text{m}$  and molecular lines

Peaks	HCN(J = 3-2) (K km s <sup>-1</sup> )	HCO <sup>+</sup> (J = 3-2) (K km s <sup>-1</sup> )	<sup>12</sup> CO(J = 3-2) (K km s <sup>-1</sup> )	24 $\mu\text{m}$ (mJy arcsec <sup>-2</sup> )
1	5.0 $\pm$ 0.8	5.5 $\pm$ 0.8	100.2 $\pm$ 1.8	114.49 $\pm$ 1.64
2	4.1 $\pm$ 0.8	3.6 $\pm$ 0.8	72.2 $\pm$ 1.8	113.82 $\pm$ 1.64
3	4.3 $\pm$ 0.8	4.4 $\pm$ 0.8	146.7 $\pm$ 1.8	102.97 $\pm$ 1.56
4	3.9 $\pm$ 0.8	4.7 $\pm$ 0.8	100.4 $\pm$ 1.8	82.95 $\pm$ 1.40
5	4.0 $\pm$ 0.8	3.1 $\pm$ 0.8	75.7 $\pm$ 1.8	77.99 $\pm$ 1.35
6	3.2 $\pm$ 0.8	2.9 $\pm$ 0.8	72.4 $\pm$ 1.8	56.66 $\pm$ 1.15
7	3.9 $\pm$ 0.8	5.4 $\pm$ 0.8	99.0 $\pm$ 1.8	85.99 $\pm$ 1.42
8	12.3 $\pm$ 0.8	5.6 $\pm$ 0.8	190.1 $\pm$ 1.8	68.91 $\pm$ 1.27

Note. — We show the low resolution (6'') intensity of the nucleus and ring, as well as the Spitzer 24 $\mu\text{m}$  continuum emission. The unit of the flux density of 24 $\mu\text{m}$  continuum emission is mJy arcsec<sup>-2</sup> (10<sup>-3</sup> erg s<sup>-1</sup> cm<sup>-1</sup> arcsec<sup>-2</sup> Hz<sup>-1</sup>) integrated over 6''.



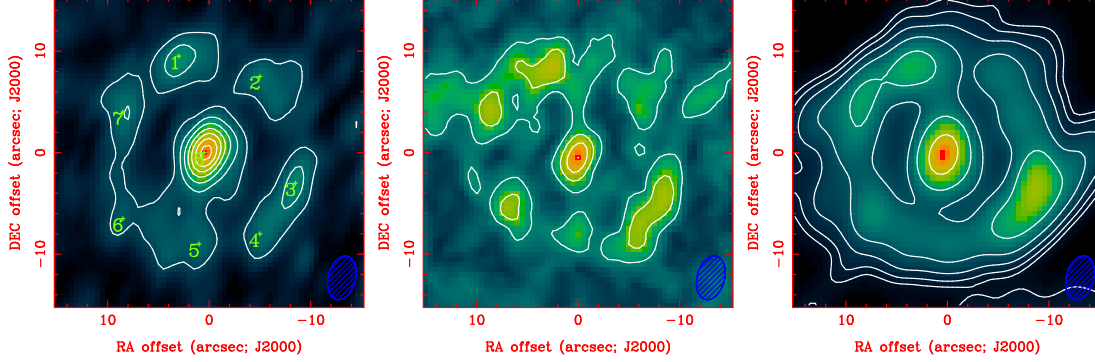


Fig. 1.— Left:  $\text{HCN}(J = 3-2)$  integrated intensity map, the contours levels are, 2, 4, 6, 8, 10, 12,  $14\sigma$ , where  $1\sigma$  is  $1.2 \text{ Jy beam}^{-1} \text{ km s}^{-1}$ . Middle:  $\text{HCO}^+(J = 3-2)$  integrated intensity map, the contours levels are, 2, 4,  $6\sigma$ , where  $1\sigma$  is  $1.2 \text{ Jy beam}^{-1} \text{ km s}^{-1}$ . Right:  $^{12}\text{CO}(J = 3-2)$  integrated intensity map, the contours levels are, 2, 4, 8, 16, 32,  $64\sigma$ , where  $1\sigma$  is  $4.5 \text{ Jy beam}^{-1} \text{ km s}^{-1}$ . The synthesized beam of the three images are  $4''.4 \times 2''.7$  ( $\text{PA} = -14.6^\circ$ ).

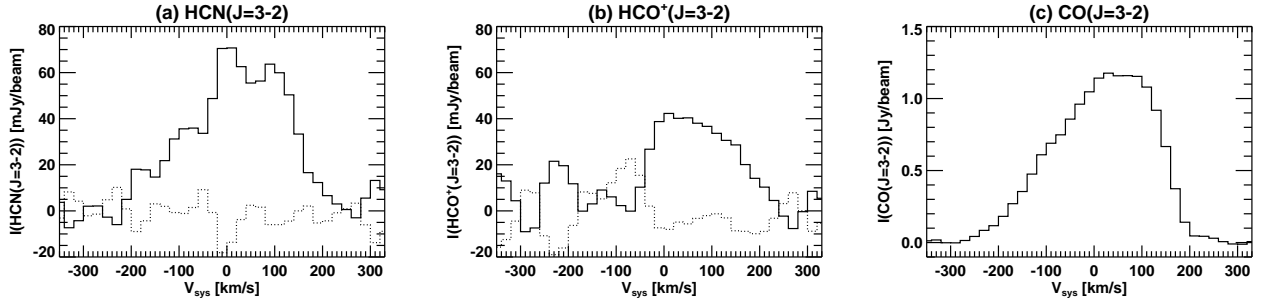


Fig. 2.— (a)  $\text{HCN}(J = 3-2)$  spectrum of the nucleus (solid-line). We subtract the  $\text{HCN}(J = 3-2)$  spectrum by CO spectrum (Fig.2c) as template to check whether the residuals (dotted-line) are significant. The CO spectrum is multiplied by 0.05 for the subtraction. (b)  $\text{HCO}^+(J = 3-2)$  spectrum of the nucleus (solid-line). We subtract the  $\text{HCO}^+(J = 3-2)$  spectrum by CO spectrum as template to check whether the residuals (dotted-line) are significant. The CO spectrum is multiplied by 0.03 for the subtraction. (c)  $\text{CO}(J = 3-2)$  spectrum of the nucleus. The synthesized beam of all the spectra are  $4''.4 \times 2''.7$  ( $\text{PA} = -14.6^\circ$ )

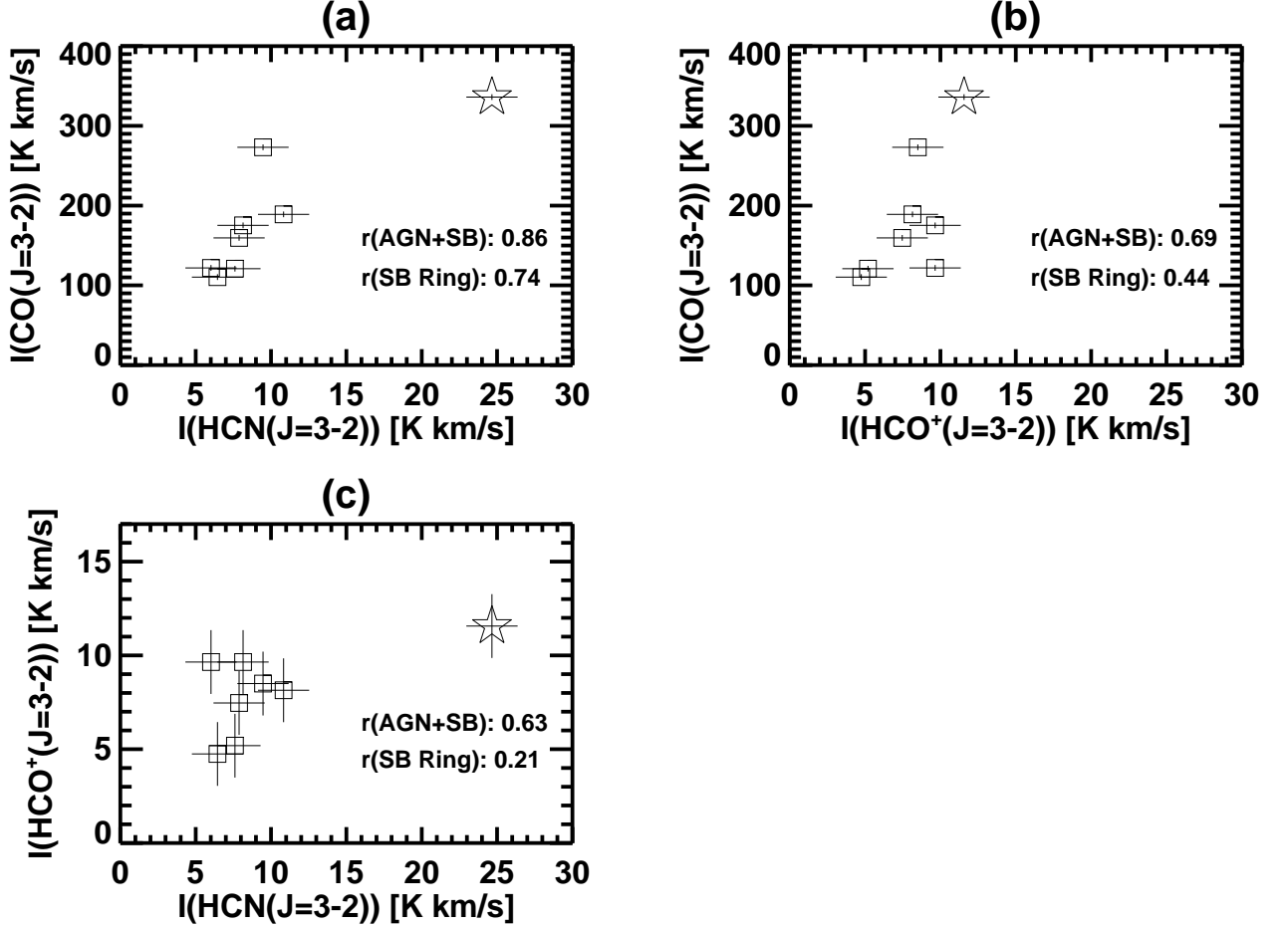


Fig. 3.— (a) The correlation of  $\text{HCN}(J = 3-2)$  and  $^{12}\text{CO}(J = 3-2)$  line intensity. The fluxes of the GMAs in the ring are shown as squares, and star represents the data of the nucleus. The units are  $\text{K km s}^{-1}$ . The  $\pm 1\sigma$  uncertainties are overlaid on the symbols with vertical/horizontal bars. The linear Pearson coefficients are shown in the plots.  $r(\text{AGN+SB})$  are the coefficients of all data, and  $r(\text{SB Ring})$  are derived for the starburst ring GMAs only. (b) The correlation of  $\text{HCO}^+(J = 3-2)$  and  $^{12}\text{CO}(J = 3-2)$  line intensity. (c) The correlation of  $\text{HCN}(J = 3-2)$  and  $\text{HCO}^+(J = 3-2)$ . The symbols are the same as (a). The data we show here are from resolution of  $4''.4 \times 2''.7$ .

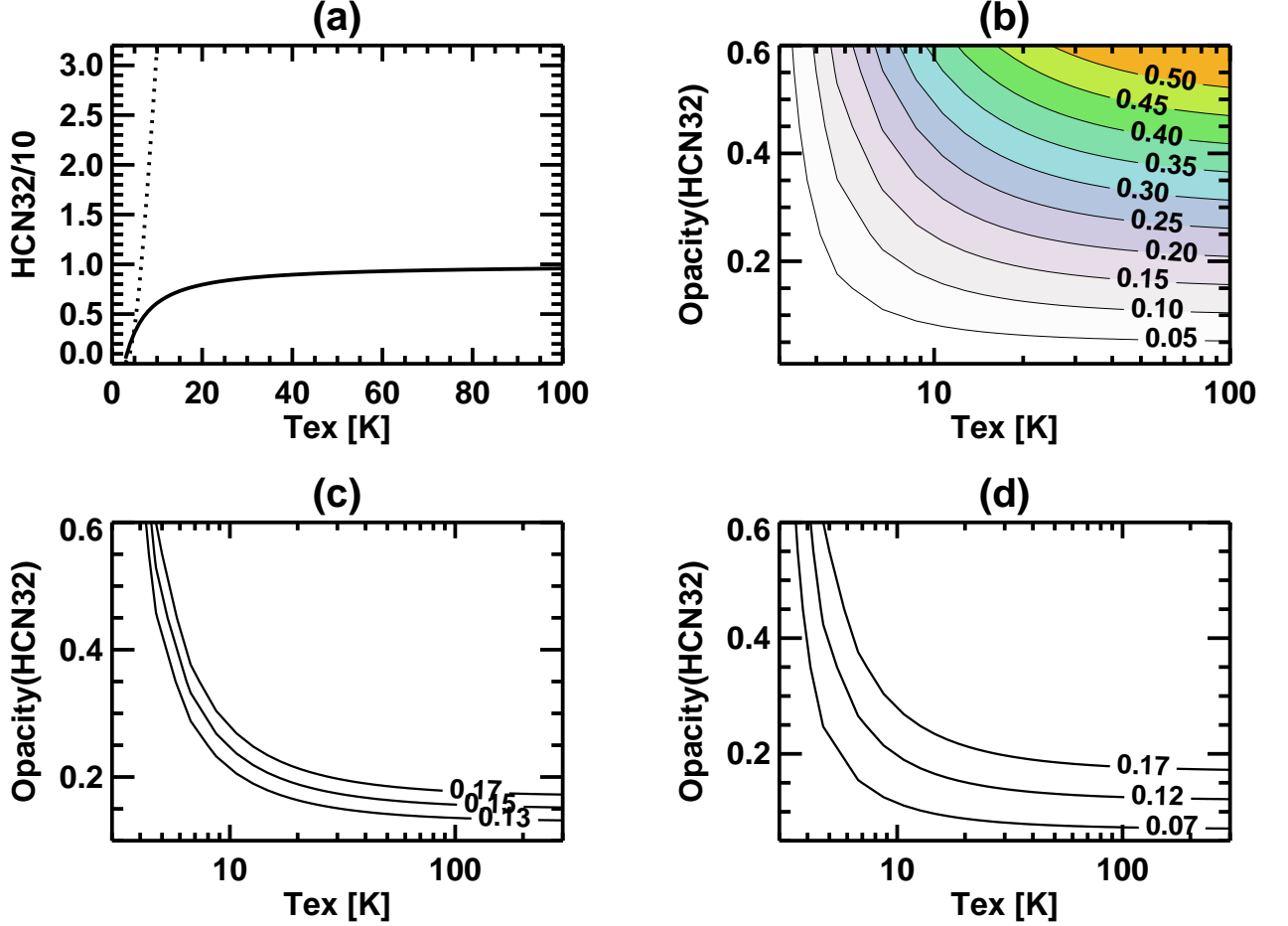


Fig. 4.— (a) The  $\text{HCN}(J = 3-2)/\text{HCN}(J = 1-0)$  intensity ratio as a function of excitation temperature in LTE conditions. The solid line is for when both lines are optically thick. The dotted line is for when both lines are optically thin. (b) The  $\text{HCN}(J = 3-2)/\text{HCN}(J = 1-0)$  intensity ratio as a function of excitation temperature and  $\tau_{\text{HCN}32}$  in LTE conditions. In this case, the  $\text{HCN}(J = 3-2)$  is thin and  $\text{HCN}(J = 1-0)$  is thick. The ratios are shown as contours from 0.05 to 0.5 in steps of 0.05. (c) The  $\text{HCN}(J = 3-2)/\text{HCN}(J = 1-0)$  ratios of the nucleus  $0.15 \pm 0.02$  shown as a function of the  $T_{\text{ex}}$  and  $\tau_{\text{HCN}32}$ . (d) The  $\text{HCN}(J = 3-2)/\text{HCN}(J = 1-0)$  ratios of the ring  $0.12 \pm 0.05$  shown as a function of the  $T_{\text{ex}}$  and  $\tau_{\text{HCN}32}$ .

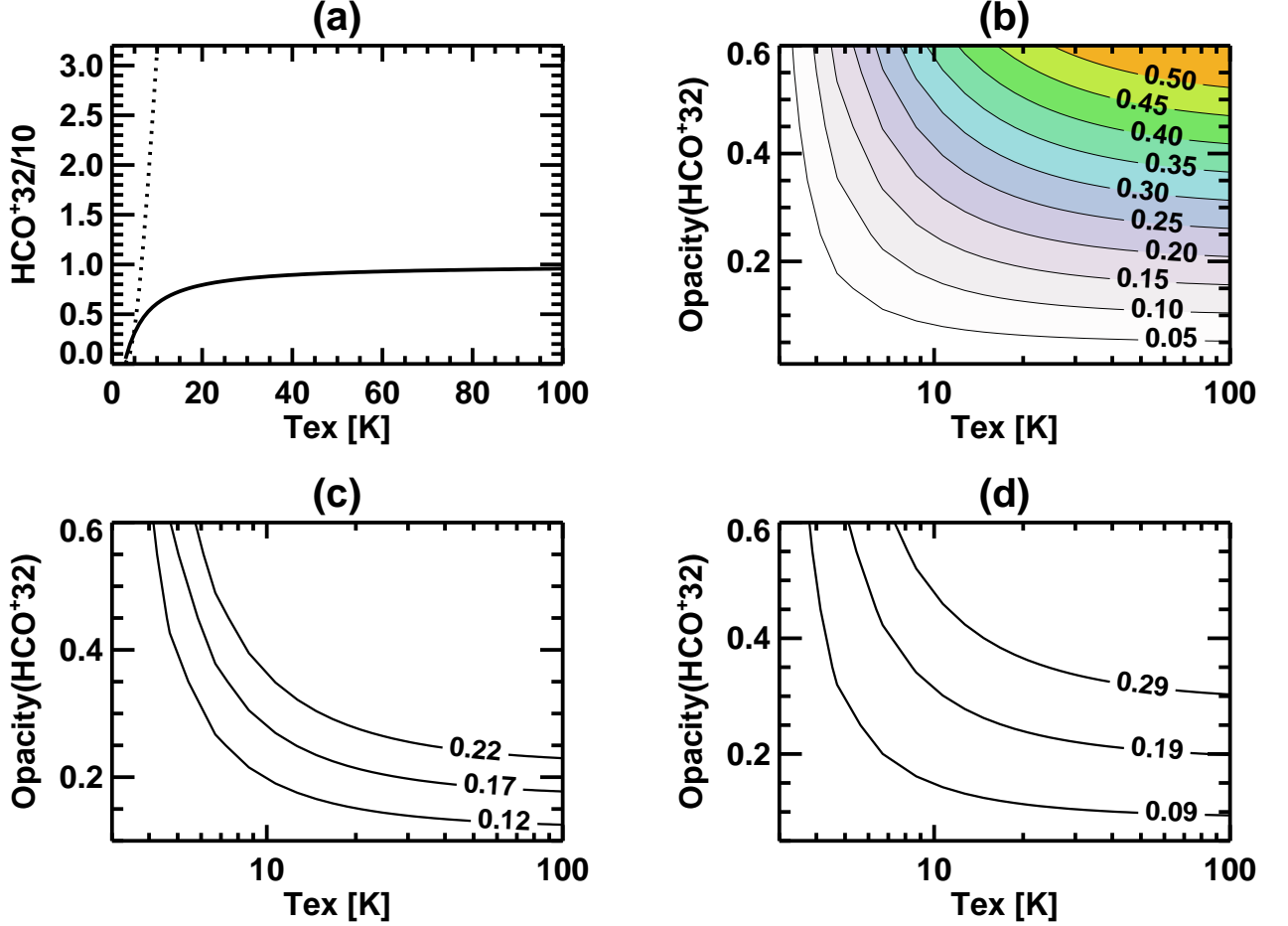


Fig. 5.— (a) The  $\text{HCO}^+(J = 3-2)/\text{HCO}^+(J = 1-0)$  intensity ratio as a function of excitation temperature in LTE conditions. The solid line is for when both lines are optically thick. The dotted line is for when both lines are optically thin. (b) The  $\text{HCO}^+(J = 3-2)/\text{HCO}^+(J = 1-0)$  intensity ratio as a function of excitation temperature and  $\tau_{\text{HCO}^+_{32}}$  in LTE conditions. In this case, the  $\text{HCO}^+(J = 3-2)$  is thin and  $\text{HCO}^+(J = 1-0)$  is thick. The ratios are shown as contours from 0.05 to 0.5 in steps of 0.05. (c) The  $\text{HCO}^+(J = 3-2)/\text{HCO}^+(J = 1-0)$  ratios of the nucleus  $0.17 \pm 0.05$  shown as a function of the  $T_{\text{ex}}$  and  $\tau_{\text{HCO}^+_{32}}$ . (d) The  $\text{HCO}^+(J = 3-2)/\text{HCO}^+(J = 1-0)$  ratios of the ring  $0.19 \pm 0.10$  shown as a function of the  $T_{\text{ex}}$  and  $\tau_{\text{HCO}^+_{32}}$ .

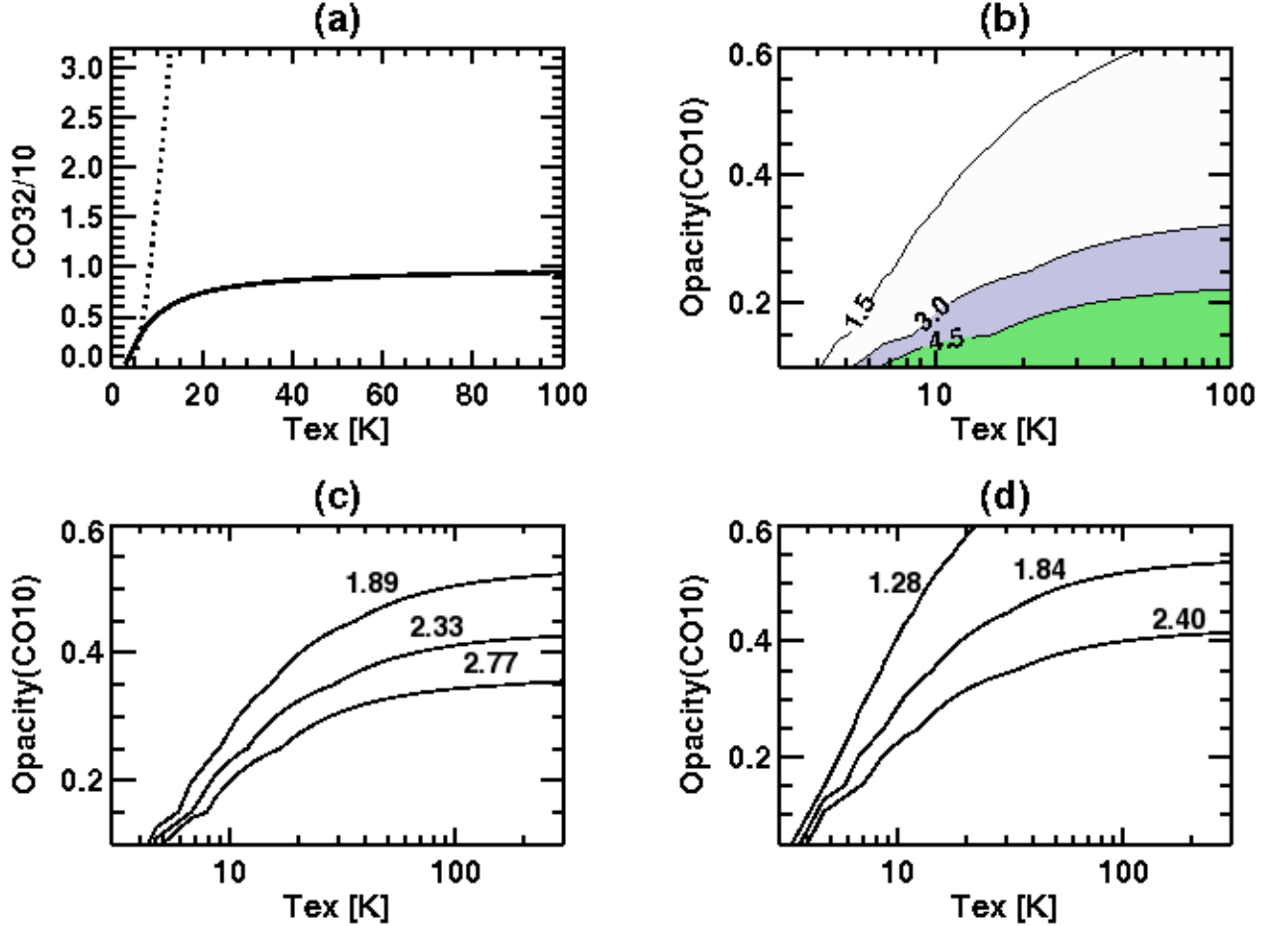


Fig. 6.— (a) The  $^{12}\text{CO}(J = 3-2)/^{12}\text{CO}(J = 1-0)$  intensity ratio as a function of excitation temperature in LTE conditions. The solid line is for when both lines are optically thick. The dotted line is for when both lines are optically thin. (b) The  $^{12}\text{CO}(J = 3-2)/^{12}\text{CO}(J = 1-0)$  intensity ratio as a function of excitation temperature and  $\tau_{\text{CO}10}$  in LTE conditions. In this case, the  $^{12}\text{CO}(J = 1-0)$  line is thin and  $^{12}\text{CO}(J = 3-2)$  line is thick. The ratios are shown as contours higher than unity, from 1.5, 3, and 4.5 to illustrate the dependence of the opacity and  $T_{\text{ex}}$ . (c) The  $^{12}\text{CO}(J = 3-2)/^{12}\text{CO}(J = 1-0)$  ratios of the nucleus  $2.33 \pm 0.44$  shown as a function of the  $T_{\text{ex}}$  and  $\tau_{\text{CO}10}$ . (d) The  $^{12}\text{CO}(J = 3-2)/^{12}\text{CO}(J = 1-0)$  ratios of the ring  $1.84 \pm 0.56$  shown as a function of the  $T_{\text{ex}}$  and  $\tau_{\text{CO}10}$ .



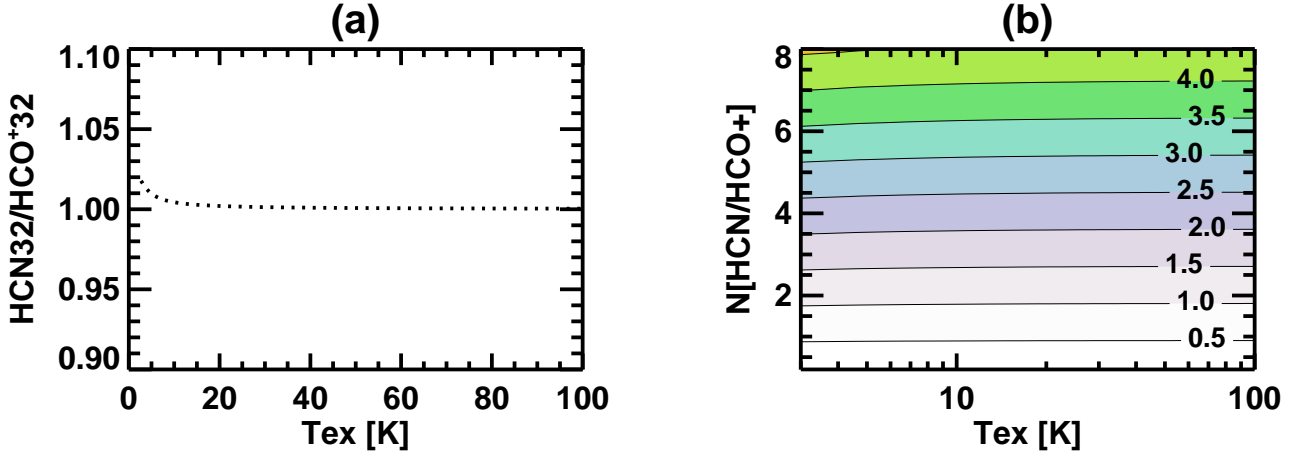


Fig. 7.— (a) The  $\text{HCN}(J = 3-2)/\text{HCO}^{+}(J = 3-2)$  intensity ratios as a function of excitation temperature in LTE conditions. In this case both lines are optically thick. The ratios are nearly unity. (b) The  $\text{HCN}(J = 3-2)/\text{HCO}^{+}(J = 3-2)$  intensity ratios (contours) as a function of excitation temperature and abundance ratios of  $\text{HCN}/\text{HCO}^{+}$  in LTE conditions. The ratios of the contours are labeled. In this case, both lines are optically thin.

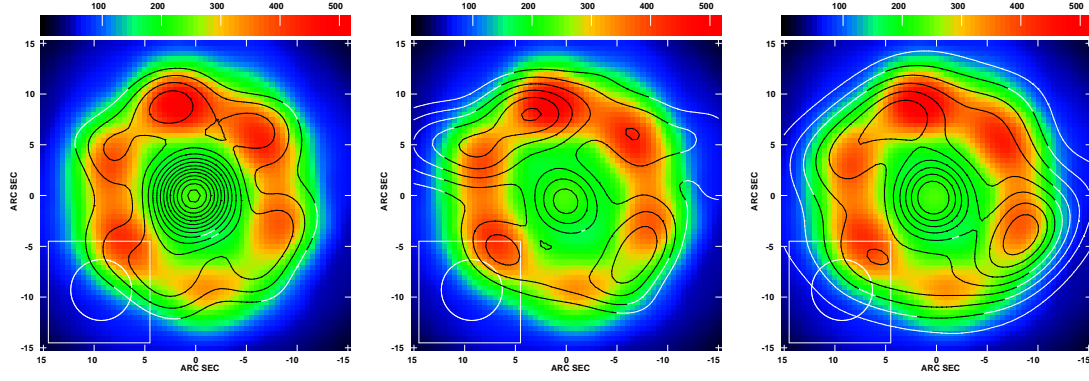


Fig. 8.— Left: The  $\text{HCN}(J = 3-2)$  map is overlaid on the  $24\mu\text{m}$  continuum map. Middle: The  $\text{HCO}^+(J = 3-2)$  map is overlaid on the  $24\mu\text{m}$  continuum map. Right: The  $\text{CO}(J = 3-2)$  map is overlaid on the  $24\mu\text{m}$  continuum map. The resolutions of the  $\text{HCN}(J = 3-2)$  and  $\text{HCO}^+(J = 3-2)$  are matched to that of the PSF of the  $24\mu\text{m}$  continuum map ( $6''$ ). The contour starts from  $4.50 \text{ Jy Beam}^{-1} \text{ km s}^{-1}$ , and in steps of  $1.50 \text{ Jy Beam}^{-1} \text{ km s}^{-1}$ .

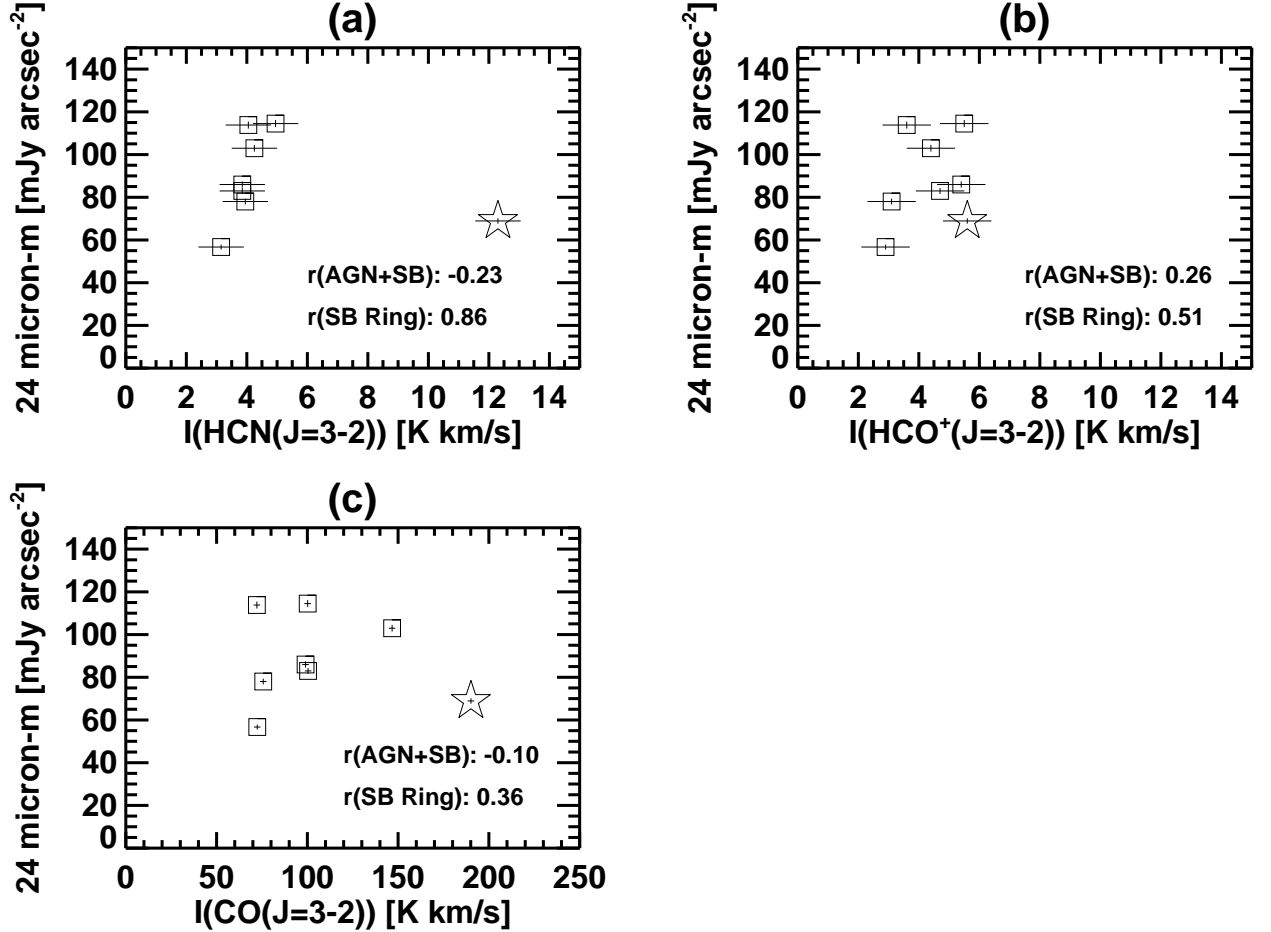


Fig. 9.— (a) The correlation of HCN( $J = 3-2$ ) integrated intensity and  $24\mu\text{m}$  continuum flux. The symbols are the same as Figure 3. The  $\pm 1\sigma$  uncertainties are overlaid on the symbols with vertical/horizontal bars. The linear Pearson coefficients are shown in the plots.  $r(\text{AGN+SB})$  are the coefficients of all data, and  $r(\text{SB Ring})$  are derived for the starburst ring GMAs only. (b) The correlation of HCO<sup>+</sup>( $J = 3-2$ ) integrated intensity and  $24\mu\text{m}$  continuum flux. The symbols are the same as Figure 3. (c) The correlation of <sup>12</sup>CO( $J = 3-2$ ) integrated intensity and  $24\mu\text{m}$  continuum flux. The symbols are the same as Figure 3. The flux are measured from low resolution maps ( $6''$ ).